FRONTIERS OF PHYSICS

RESEARCH ARTICLE
Volume 18 / Issue 4 / 44301 / 2023

Interpretations of the cosmic ray secondary-to-primary ratios measured by DAMPE

Peng-Xiong Ma[1], Zhi-Hui Xu[1,2], Qiang Yuan[1,2,†], Xiao-Jun Bi[3,4], Yi-Zhong Fan[1,2], Igor V. Moskalenko[5], Chuan Yue[1]

1 Key Laboratory of Dark Matter and Space Astronomy, Purple Mountain Observatory, Chinese Academy of Sciences, Nanjing 210023, China
2 School of Astronomy and Space Science, University of Science and Technology of China, Hefei 230026, China
3 Key Laboratory of Particle Astrophysics, Institute of High Energy Physics, Chinese Academy of Sciences, Beijing 100049, China
4 University of Chinese Academy of Sciences, Beijing 100049, China
5 W. W. Hansen Experimental Physics Laboratory and Kavli Institute for Particle Astrophysics and Cosmology, Stanford University, Stanford, CA 94305, USA
Corresponding author. E-mail: †yuanq@pmo.ac.cn
Received November 1, 2022; accepted December 25, 2022

ABSTRACT

Precise measurements of the boron-to-carbon and boron-to-oxygen ratios by DAMPE show clear hardenings around 100 GeV/n, which provide important implications on the production, propagation, and interaction of Galactic cosmic rays. In this work we investigate a number of models proposed in literature in light of the DAMPE findings. These models can roughly be classified into two classes, driven by propagation effects or by source ones. Among these models discussed, we find that the re-acceleration of cosmic rays, during their propagation, by random magnetohydrodynamic waves may not reproduce sufficient hardenings of B/C and B/O, and an additional spectral break of the diffusion coefficient is required. The other models can properly explain the hardenings of the ratios. However, depending on simplifications assumed, the models differ in their quality in reproducing the data in a wide energy range. The models with significant re-acceleration effect will under-predict low-energy antiprotons but over-predict low-energy positrons, and the models with secondary production at sources over-predict high-energy antiprotons. For all models high-energy positron excess exists.

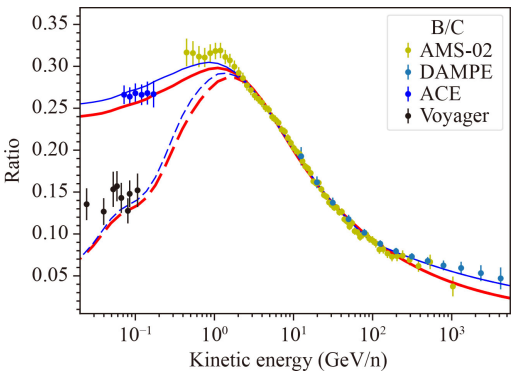

Keywords cosmic rays, propagation

1 Introduction

Galactic cosmic rays (GCRs) are energetic particles produced by powerful astrophysical objects such as the remnants of supernova explosions. After being accelerated up to very high energies, they propagate and interact in the Milky Way before entering the solar system and being recorded by our detectors. There are typically two types of GCRs, the primary family (such as protons, helium, carbon, oxygen, neon, magnesium, silicon, and iron) which is produced directly by acceleration at their sources and the secondary family (such as lithium, berylium, boron, and sub-iron nuclei) which is produced via fragmentations of primary particles mainly during

Higher Education Press

arXiv: 2210.09205
https://doi.org/10.1007/s11467-023-1257-7

the propagation process. Precise measurements of the ratios between secondary particles and their parent primary particles are important probe of the propagation of GCRs as well as the turbulent properties of the interstellar medium (ISM) [1–3].

Among various secondary-to-primary ratios of nuclei, the boron-to-carbon ratio (B/C) is the best measured and most widely studied. Measurements of B/C up to kinetic energies[1)] of hundreds of GeV/n have been achieved with good precision by many experiments [4–16], which were extensively used to constrain the propagation of GCR models (e.g., [17–30]). The B/C ratio above $O(10)$ GV can be well fitted by a power-law function of rigidity, $\propto \mathcal{R}^{-\delta}$, with $\delta \approx 1/3$ [12], in agreement with the prediction of GCR diffusion in the ISM with a Kolmogorov type turbulence spectrum [18, 31]. Further measurements of ratios of secondary lithium, beryllium, and boron to primary carbon and oxygen by AMS-02 jointly showed a hardening [4, 32]. Non-trivial spectral shapes of the secondary-to-primary ratios thus challenge the simple production and propagation models of GCRs.

Very recently, high-precision measurements up to 5 TeV/n of the boron-to-carbon (B/C) and boron-to-oxygen (B/O) ratios have been obtained by the Dark Matter Particle Explorer (DAMPE; [33, 34]). The DAMPE results revealed clear hardening of both ratios with high significance at nearly the same kinetic energy of ~ 100 GeV/n [35]. A broken power-law fit to the B/C (B/O) ratio gives a low-energy slope of 0.356 (0.394) and a high-energy slope of 0.201 (0.187), and the change of slope is $\Delta\gamma = 0.155$ (0.207). Previous measurements showed also remarkable hardenings of primary nuclei at similar energies [36–42]. The slope changes of primary nuclei are about 0.1–0.2, which are slightly diverse among different measurements. These spectral features of GCRs may suggest a common origin.

A straightforward interpretation of the hardenings of B/C and B/O is the existence of a break of the diffusion coefficient at a few hundred GV [43–45]. Such a break of the diffusion coefficient may be a consequence of the change of the scale-dependence of the ISM turbulence, or be due to the nonlinear particle-wave interactions [46]. Other interpretations with different physical models were also proposed (e.g., [47–53]). These models either employ more complicated propagation effects or introduce additional sources of (secondary and/or primary) GCRs beyond the standard paradigm. Some of the above possibilities have been briefly discussed in Ref. [35]. In this work we further explore these models to test whether they can explain the DAMPE data satisfactorily. Antiprotons and positrons from these models will also be discussed as independent tests of the models.

[1)] In this paper, we are necessarily using the mixed energy units: discussions of the injection spectra and cosmic ray transport is done in terms of rigidity, while a comparison with experiments requires a conversion to the kinetic energy per nucleon.

2 Production and propagation model of galactic cosmic rays

The propagation of GCRs in the Milky Way can be generally described by the diffusion equation

$$\frac{\partial \psi}{\partial t} = \nabla \cdot (D_{xx} \nabla \psi - \boldsymbol{V}_c \psi) + \frac{\partial}{\partial p} p^2 D_{pp} \frac{\partial}{\partial p} \frac{1}{p^2} \psi - \frac{\partial}{\partial p} \left[\dot{p} \psi - \frac{p}{3} (\nabla \cdot \boldsymbol{V}_c \psi) \right] - \frac{\psi}{\tau_f} - \frac{\psi}{\tau_r} + q(\boldsymbol{r}, p) \,, \tag{1}$$

which includes also the possible convective transportation effect with velocity $\boldsymbol{V}_c$, the re-accerlation effect described by a diffusion in the momemtum space with diffusion coefficient D_{pp}, the energy losses with rate $\dot{p}$ and adiabatic losses, fragmentations with time scale τ_f, and radioactive decays with lifetime τ_r [54]. The source function $q(\boldsymbol{r}, p)$ includes both the primary contribution from acceleration sources and the secondary contribution from GCR interactions with the ISM.

The geometry of the propagation halo is assumed to be cynlindrially symmetric, with radial extension $R_h = 20$ kpc and height $\pm z_h$ to be determined by the data. The spatial diffusion coefficient is usually assumed to be spatially homogeneous, and depends on particle rigidity with a power-law form:

$$D_{xx}(\mathcal{R}) = D_0 \beta^\eta \left(\frac{\mathcal{R}}{\mathcal{R}_0} \right)^\delta , \tag{2}$$

where β is the velocity of the particle in unit of light speed, $\mathcal{R}_0 \equiv 4$ GV is a reference rigidity, δ is the power-law index describing the properties of the interstellar turbulence. A phenomenological parameter η is introduced to modify the velocity dependence at low energies, in order to better match the measurements. We will discuss alternative cases about the diffusion coefficient in this work (see below Section 3 for details). The convection effect is neglected in this work according to the fitting to the up-to-date data on GCR primary and secondary nuclei [17, 55]. The momentum diffusion coefficient can be expressed as [56]

$$D_{pp} = \frac{4 p^2 v_A^2}{3\delta(4-\delta^2)(4-\delta) w D_{xx}}, \tag{3}$$

where v_A is the Alfven speed of magnetized disturbances, w is the ratio of magnetohydrodynamic (MHD) wave energy density to the magnetic field energy density and can be effectively absorbed into v_A.

The injection spectrum is assumed to be a smoothly broken power-law function of rigidity

$$q(\mathcal{R}) = q_0 \mathcal{R}^{-\gamma_0} \prod_{i=1}^{n} \left[1 + \left(\frac{\mathcal{R}}{\mathcal{R}_{\mathrm{br},i}} \right)^s \right]^{(\gamma_{i-1}-\gamma_i)/s} , \tag{4}$$

where γ_0 is the spectral index at the lowest energies, γ_{i-1} and γ_i are spectral indices below and above break rigidity $\mathcal{R}_{\mathrm{br},i}$, and s describes the smoothness of the break which was fixed to be $s=2$ throughout this work. Depending on the assumptions and purposes of different models, different numbers of breaks will be assumed. Specifically, $n=2$ will be assumed in general, except that the high-energy hardening is ascribed to other physical effects ($n=1$ in these cases). The spatial distribution of sources of GCRs is parameterized as

$$f(r,z)=\left(\frac{r}{r_\odot}\right)^{\alpha}\exp\left[-\frac{\beta(r-r_\odot)}{r_\odot}\right]\exp\left(-\frac{|z|}{z_s}\right), \quad (5)$$

where $r_\odot=8.5$ kpc is the distance from the solar system to the Galactic center, $z_s=0.2$ kpc is the scale width of the vertical extension of sources, $\alpha=1.25$, and $\beta=3.56$ [24]. Unless explicitly stated, we will use the GALPROP[2)] code (version 56[3)]) to calculate the propagation of GCRs [18].

To compare with the low-energy measurements in the solar system, we use the force-field approximation to account for the solar modulation of GCRs [58]. More sophisticated models of heliospheric propagation exist, e.g., HELMOD [59], but using them is beyond the scope of this paper.

3 Interpretations of spectral breaks of B/C and B/O

3.1 Nested leaky box model

The leaky-box model, which was popular for the most part of the 20th century, is a simplified model with uniform distribution of gas, sources, and cosmic rays where the cosmic ray transport in the whole Galaxy is described with a single parameter, the escape time $\tau_{\mathrm{esc}}(\mathcal{R})$. Neglecting other processes such as the convection, re-acceleration, and fragmentation, the solution of the propagation equation is as simple as $\psi(\mathcal{R})=q(\mathcal{R})\tau_{\mathrm{esc}}(\mathcal{R})$. An extension of the leaky box model to take into account the residence and secondary production in dense regions surrounding the sources, known as the nested leaky box (NLB) model (denoted as model A), was proposed to explain more complicated observational properties of GCRs [47, 60, 61]. In the NLB model, GCRs were accelerated to a power-law spectrum $\mathcal{R}^{-\gamma}$, which diffuse in an energy-dependent way in the immediate vicinity of the sources (so-called cocoons), and then enter the Galaxy and finally leak to the extragalactic space in an energy-independent way. The escape time is assumed to be [47]

$$\begin{cases} \tau^{\mathrm{c}}_{\mathrm{esc}} &= \tau_1\mathcal{R}^{-\zeta\ln\mathcal{R}}, & \text{for cocoons,}\\ \tau^{\mathrm{g}}_{\mathrm{esc}} &= \tau_2\equiv\text{const}, & \text{for Galaxy.}\end{cases} \quad (6)$$

For primary GCRs, the propagated spectrum in cocoons is $\psi^{\mathrm{c}}_{\mathrm{pri}}(\mathcal{R})=q(\mathcal{R})\tau^{\mathrm{c}}_{\mathrm{esc}}\propto\mathcal{R}^{-\gamma-\zeta\ln\mathcal{R}}$. The propagated spectrum in the Galaxy is $\psi^{\mathrm{g}}_{\mathrm{pri}}(\mathcal{R})=[\psi^{\mathrm{c}}_{\mathrm{pri}}/\tau^{\mathrm{c}}_{\mathrm{esc}}]\tau^{\mathrm{g}}_{\mathrm{esc}}=q(\mathcal{R})\tau^{\mathrm{g}}_{\mathrm{esc}}\propto\mathcal{R}^{-\gamma}$, whose spectral shape is the same as the source spectrum. For secondary particles, there are two components. The one in cocoons has a spectrum $\psi^{\mathrm{c}}_{\mathrm{sec}}=\psi^{\mathrm{c}}_{\mathrm{pri}}\cdot n_{\mathrm{c}}\sigma v\cdot\tau^{\mathrm{c}}_{\mathrm{esc}}$. This component then injects into the Galaxy and experiences a further leakage, resulting in a final spectrum $\psi^{\mathrm{c,g}}_{\mathrm{sec}}=[\psi^{\mathrm{c}}_{\mathrm{sec}}/\tau^{\mathrm{c}}_{\mathrm{esc}}]\tau^{\mathrm{g}}_{\mathrm{esc}}$. The other component is directly produced by GCRs in the Galaxy, whose spectrum is $\psi^{\mathrm{g,g}}_{\mathrm{sec}}=\psi^{\mathrm{g}}_{\mathrm{pri}}\cdot n_{\mathrm{g}}\sigma v\cdot\tau^{\mathrm{g}}_{\mathrm{esc}}$. The total secondary spectrum is thus $\psi^{\mathrm{g}}_{\mathrm{sec}}=\psi^{\mathrm{c,g}}_{\mathrm{sec}}+\psi^{\mathrm{g,g}}_{\mathrm{sec}}=q(\mathcal{R})\tau^{\mathrm{g}}_{\mathrm{esc}}\sigma v(n_{\mathrm{c}}\tau^{\mathrm{c}}_{\mathrm{esc}}+n_{\mathrm{g}}\tau^{\mathrm{g}}_{\mathrm{esc}})$. In the above formulae, n_{c} and n_{g} are the gas densities in cocoons and the Galaxy, σ is the production cross section, and v is the velocity of the GCR particle.

Here we set $n_{\mathrm{c}}=1$ H·cm^{-3}, $n_{\mathrm{g}}=0.1$ H·cm^{-3}, and derive the other parameters through fitting to the data. Since some complicated physical effects at low energies (e.g., the ionization and Coulomb energy losses) are not included in the NLB model, we focus on the data-model comparison above a few tens of GeV/n. Several experiments found that the spectra of carbon and oxygen nuclei are not single power-law, but experience hardening features around a few hundred GV [36–39]. We therefore assume that the source spectrum is a smoothly broken power-law form of rigidity with $n=1$ in Eq. (4).

Figure 1 shows the best-fit B/C, B/O, and C, O fluxes in the NLB model, compared with the AMS-02 [4, 38] and DAMPE [35] data, where the statistical and systematic errors of the measurements are added in quadrature. The fitting parameters are $\gamma_0=2.69\pm0.01$, $\mathcal{R}_{\mathrm{br},1}=(533\pm292)$ GV, $\gamma_1=2.54\pm0.07$ for C, and $\gamma_0=2.67\pm0.01$, $\mathcal{R}_{\mathrm{br},1}=(864\pm637)$ GV, $\gamma_1=2.51\pm0.11$ for O. For the secondary-to-primary ratios, we have $\tau_1\sigma=(9.42\pm0.43)\times10^{-12}$ cm^2·s, $\tau_2\sigma=(1.88\pm0.06)\times10^{-11}$ cm^2·s, $\zeta=-0.07$ for the B/C ratio, and $\tau_1\sigma=(1.04\pm0.06)\times10^{-11}$ cm^2·s, $\tau_2\sigma=(1.84\pm0.06)\times10^{-11}$ cm^2·s, $\zeta=-0.08$ for the B/O ratio. There are many channels to produce boron from fragmentations of carbon and oxygen [62, 63]. As an order of magnitude estimate, we take the total fragmentation cross section of carbon, ~250 mb, as a reference and obtain $\tau_1\sim1.3$ Myr and $\tau_2\sim2.3$ Myr.

In the NLB model, the high-energy behaviors of B/C and B/O asymptotically approach constants due to the energy-independent leakage in the Milky Way. This energy-independent leakage predicts a constant dipole anisotropy[4)] of GCRs above ~TeV [61], which is at odds with observations. The NLB model is over-simplified, neglecting many important processes of propagation of

[2)]Webpage: galprop.stanford.edu

[3)]A newer version 57 was recently released [57].

[4)]The density gradient is ignored in the leaky box model. Via an analogy with the diffusion model with diffusion coefficient being scaled to the escape time, the anisotropy in this model was estimated.

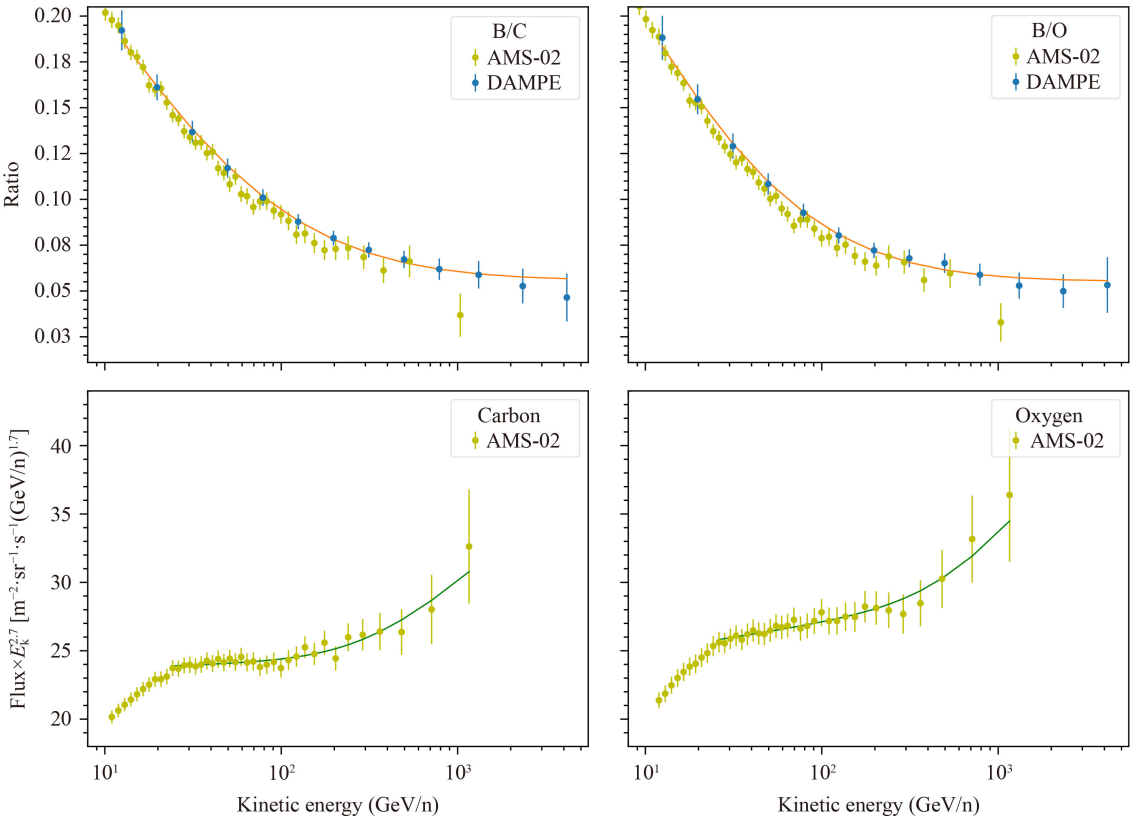

Fig. 1 B/C and B/O ratios (top panels), and C, O fluxes (bottom panels) for the NLB model.

GCRs, and fails to reproduce data in a wide energy range. However, the idea that GCRs may propagate differently in different regions is important and will be extended to a spatially-dependent propagation model or a scenario with confinements and interactions surrounding the acceleration sources detailed below.

3.2 Re-acceleration during propagation

GCR particles may get re-accelerated via interactions with randomly moving interstellar MHD waves during their propagation process [56]. This stochastic acceleration process is usually described by a diffusion in momentum space, with diffusion coefficient D_{pp}. The re-acceleration results in bump-like spectral features of low-energy (less than tens of GeV/n) GCRs, and was shown can better explain the peaks of secondary-to-primary ratios [17, 55, 64]. The softer spectra of secondary nuclei experience larger effect of re-acceleration, leading to a decrease in the secondary-to-primary ratio at low energies. Fitting to the new measurements of the Li, Be, B, C, and O fluxes by AMS-02 [4, 38] indicates that the re-acceleration can indeed reproduce well the reported more significant hardenings of the secondary family than the primary family [48]. We re-visit the question whether the re-acceleration can explain the even stronger hardenings of the B/C and B/O ratios measured by DAMPE.

The fitting procedure is similar with Ref. [48]. We include the Voyager measurements outside the solar system [14], the 5-year AMS-02 secondary-to-primary data and 5-year carbon and oxygen data [4, 38], the ACE-CRIS[5)] measurements with the same time period of AMS-02, and the DAMPE data. To reduce the degeneracy between the diffusion coefficient and the halo height, the data of $_{10}$Be/$_{9}$Be from several experiments are also included [65–69]. The data used in the fitting are summarized in Table 1.

We employ the Markov Chain Monte Carlo (MCMC) method to do the fitting, using the `emcee` code [70]. The injection spectrum takes the form of Eq. (4) with $n = 2$. The best-fit model parameters are given in Table 2 (labelled as model B). The red thick lines in Fig. 2 show the best-fit results of the B/C and B/O ratios (top panels), and carbon and oxygen fluxes (bottom panels). We can see that the re-acceleration effect can explain partly the hardenings of the B/C and B/O ratios, but is not enough to reproduce the DAMPE data at high energies. Therefore, we introduce an additional break for the diffusion coefficient, i.e., the rigidity-dependence slope becomes δ_h for $\mathcal{R} > \mathcal{R}_h$, and re-do the fitting. As shown

[5)] Webpage: www.srl.caltech.edu/ACE/ASC/level2/lvl2DATA_CRIS.html

Table 1 Data used in the fitting.

	Experiment	Time	Ref.
B/C	Voyager	2012/12-2015/06	[14]
	ACE	2011/05-2016/05	[55]
	AMS-02	2011/05-2016/05	[4]
	DAMPE	2016/01-2021/12	[35]
B/O	ACE	2011/05-2016/05	
	AMS-02	2011/05-2016/05	[4]
	DAMPE	2016/01-2021/12	[35]
C & O	Voyager	2012/12-2015/06	[14]
	ACE	2011/05-2016/05	[55]
	AMS-02	2011/05-2016/05	[38]
^{10}Be/^{9}Be	Voyager	1977/01-1998/12	[65]
	ACE	1997/08-1999/04	[66]
	IMP	1974/01-1980/05	[67]
	Ulysses	1990/10-1997/12	[68]
	ISOMAX	1998/08-1998/08	[69]

by the blue thin lines in Fig. 2, this model (labelled as B′) matches both the ratios and fluxes much better. The best-fit model parameters are also given in Table 2. We note that γ_1 and γ_2 in this model are very close to each other, which means that the hardenings of both the primary nuclei and secondary-to-primary ratios are due to the break of the diffusion coefficient.

3.3 Re-acceleration by a nearby source

Malkov and Moskalenko proposed recently that the re-acceleration of GCRs by a close star, such as Epsilon Eridani, can well explain the observed bump structures of GCRs [49, 71]. This scenario predicts hardenings of both primary and secondary nuclei which were re-accelerated simultaneously. Different from the stachastic acceleration in the ISM described in the previous subsection (where the impacts are mainly at low energies, e.g., for rigidity below tens of GV), this model mainly affects the GCR spectra above TV rigidities since low-energy re-accelerated particles are convected with the ISM and do not reach the solar system. It thus gives bump-like features of the GCR spectra around 10 TV, explaining both the hardenings and consequent softenings of the spectra.

The re-accelerated spectrum of a power-law background spectrum can be described as [49]

$$f(\mathcal{R}) = q(\mathcal{R})\left[1+\frac{\gamma+2}{\lambda-\gamma}\exp\left(-\sqrt{\frac{\mathcal{R}_0}{\mathcal{R}}}-\sqrt{\frac{\mathcal{R}}{\mathcal{R}_L}}\right)\right], \quad (7)$$

where $q(\mathcal{R}) = q_0\mathcal{R}^{-\gamma}$ is the background GCR spectrum, $\mathcal{R}_0$ is a characteristic rigidity of the re-accelerated bump depending on the shock properties, $\mathcal{R}_L$ is the rigidity cutoff associated with the lateral losses, $\lambda = (r+2)/(r-1)$ with r being the shock compression ratio.

Table 2 Parameters of the models discussed in Section 3.

Model	B	B′	D	E	F	G
D_0 (10^{28} cm^2·s^{-1})	6.02	3.32	8.14	...	7.30	6.94
δ	0.40	0.46	0.60	...	0.47	0.43
z_h (kpc)	5.77	3.61	8.48	...	6.23	6.29
δ_h	...	0.25	...	...	...	...
$\mathcal{R}_h$ (GV)	...	212.5	...	...	...	...
v_A (km·s^{-1})	30.0	22.4	10.3	...	35.4	32.5
η	–0.10	–0.61	–0.42	...	–0.27	–0.33
ξ	...	...	...	...	...	...
ξ_δ	...	...	0.02	...	...	...
h (kpc)	...	...	0.41	...	...	...
τ (Myr)	...	...	...	...	0.46	0.24
$\mathcal{R}_{ac}$ (GV)	...	...	...	...	...	4.0×10^3
γ_0	0.19	0.41	0.13	0.85	0.46	0.45
γ_1	2.36	2.35	2.38	2.37	2.31	2.34
γ_2	2.34	2.42	...	...	2.15	2.18
$\mathcal{R}_{br,1}$ (GV)	0.93	1.02	1.03	1.75	1.05	1.05
$\mathcal{R}_{br,2}$ (GV)	243.2	142.3	...	...	467.0	467.0
ϕ (GV)	0.71	0.69	0.71	0.68	0.71	0.69

For the "realistic" model of Ref. [49], the fitting to the proton spectrum gives $\mathcal{R}_0 = 5.9$ TV, $\mathcal{R}_L = 224$ TV, $q = 4.2$. The same parameters can be applied to other nuclei such as helium, boron, and carbon, and good consistencies with the data were shown [49].

Figure 3 shows the comparison between the model predictions and the new measurements of B/C, B/O, and C, O fluxes of this scenario (model C), adopting the same shock parameters as in Ref. [49]. The spectral parameters of background GCRs are slightly adjusted, i.e., $\gamma = 2.76$ for carbon, 2.75 for oxygen, and 3.04 for boron. While improvement of the data-model match can be expected given a re-fitting of all the data, we find that this simple model reproduces the current measurements reasonably well.

3.4 Spatially-dependent propagation

In the conventional propagation model, the diffusion coefficient is assumed to be homogeneous throughout the Milky Way. While this model can explain most of the GCR spectra and all-sky diffuse γ-rays [54, 72], recent observations indicate that the GCR propagation is likely spatially-dependent. Very high energy extended γ-ray halos around a few pulsars observed by HAWC and LHAASO suggest that particles propagate very slowly in the ISM surrounding pulsars [73, 74]. Together with the diffusion coefficient inferred from the secondary-to-primary ratios from GCR direct measurements, the propagation of GCRs could be inhomogeneous — slow in the Galactic disk (or the vicinities of sources) and fast in the halo [75, 76]. The spatially-dependent propagation model was also employed to explain the hundreds of GV

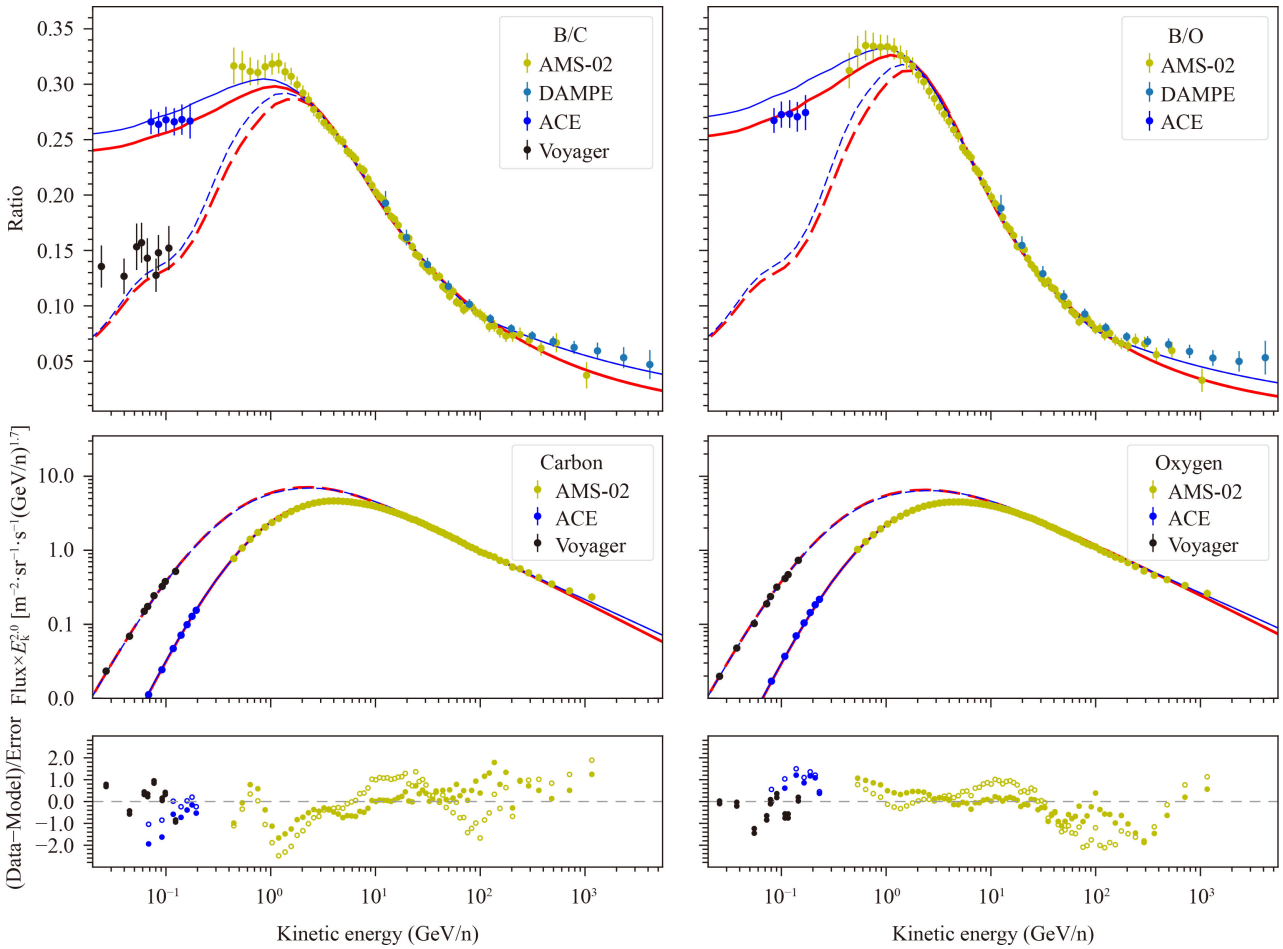

Fig. 2 B/C and B/O ratios (top panels), and C, O fluxes (bottom panels) for the re-acceleration model. Red thick lines show the results for the diffusion coefficient of Eq. (2), and blue thin lines show the results for the diffusion coefficient with an additional high-energy break. Dashed lines are the spectra in the local ISM, and solid lines are modulated spectra near the Earth. Sub-panels of bottom ones show the residuals of the model fittings to the C and O spectra. The open symbols are for model B and filled symbols are for model B,.

hardenings of GCR spectra and the high energy excess of the Fermi-LAT diffuse γ-rays [50, 77, 78]. The Bayesian analysis to derive the propagation parameters within the spatially-dependent propagation framework has also been carried out [19, 79].

We parameterize the spatial diffusion coefficient D_{xx} as

$$D_{xx}(\mathcal{R}, z) = aD_0\beta^\eta \left(\frac{\mathcal{R}}{\mathcal{R}_0}\right)^{b\delta}, \quad (8)$$

with $a = \xi + (1-\xi)[1-\exp(-z^2/(2h^2))]$, $b = \xi_\delta + (1-\xi_\delta)[1-\exp(-z^2/(2h^2))]$, where h is the characteristic thickness of the slow-diffusion disk region, ξ and ξ_δ are suppression factors of the diffusion coefficient and its rigidity-dependent slope in the disk region compared with those in the fast-diffusion halo region. The reference rigidity $\mathcal{R}_0$ is fixed to be 4 GV. Note here we ignore the possible R-dependence of the diffusion coefficient [80]. For $z \gg h$ (fast-diffusion halo), we have $a = b = 1$, and for $z \to 0$ (slow-diffusion disk), we have $a \to \xi$, $b \to \xi_\delta$.

We fit the model parameters using the same data sets and fitting procedure as in Section 3.2. In this model the hardenings at hundreds of GV are primarily ascribed to the spatially-dependent propagation effect. Hence for the injection spectrum we assume $n = 1$, where the break occurs around GV to account for the low energy data. The results are shown in Fig. 4 and Table 2. It can be seen that the model reproduces the data very well. We note that the diffusion coefficient in the disk is smaller by about three orders of magnitude than that in the halo, for a rigidity of ~ 100 TV, which is consistent with the results inferred from pulsar halo observations [73, 74]. The parameter $\xi_\delta = 0.03$ is also close to the result (~ 0) obtained in Ref. [79]. This nearly rigidity-independent diffusion coefficient in the disk may be tested by future observations of the energy-dependent morphologies of pulsar halos.

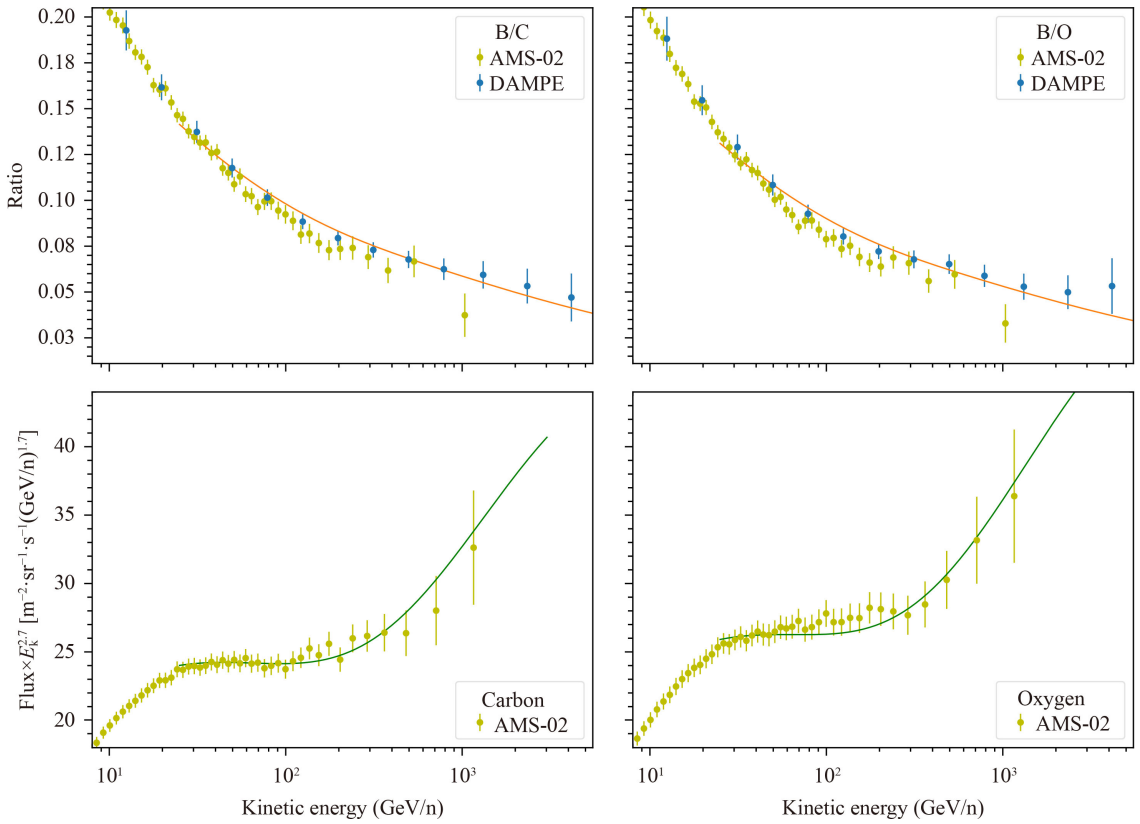

Fig. 3 B/C and B/O ratios (top panels), and C, O fluxes (bottom panels) for the model with re-acceleration by a nearby source.

3.5 Self-generated turbulence model

The GCR flows can induce MHD waves of the background plasma through the streaming instability [81], leading to self-confinement of GCRs around such waves. This nonlinear effect makes GCR propagation couples with the interstellar waves, resulting in changes of the momentum dependence and spatial dependence of the diffusion coefficient, which was employed to explain the hardening feature [46] and radial distribution [82] of GCRs. In this scenario, the break of GCR spectra around $\mathcal{R} \sim 10$ GV is due to the transition of GCR propagation from advection to the regime dominated by diffusion in self-generated turbulence, and the hardening around $\mathcal{R} \sim 200$ GV is due to a further transition of the diffusion from self-generated turbulence to externally generated turbulence [46].

A self-consistent treatment of this problem needs to solve the GCR transportation and the MHD wave evolution simultaneously. For the purpose of illustration, we simply adopt the momentum-dependence of the diffusion coefficient given in Ref. [46] and neglects its spatial variation. At low energies, the slope of the diffusion coefficient was found to be $\sim \mathcal{R}^{0.7}$, which aymptotically changes to $\sim \mathcal{R}^{1/3}$ at high energies. To better fit the data, we adjust the diffusion coefficient of Ref. [46] through multiplying a factor $a(\mathcal{R}/\mathrm{GV})^b$. The injection spectrum is again Eq. (4), with $n = 1$. We find that $a = 1.72$ and $b = -0.23$ can fit the data above a few GV relatively well, as shown in Fig. 5. The low-energy parts of the B/C and B/O ratios are over-predicted by this model. A modification of the velocity-dependence of the diffusion coefficient as in Eq. (2) may be helpful in improving the fitting.

3.6 Secondary production at sources

In the standard model, secondary particles are produced by inelastic interactions of primary GCRs with the ISM during the propagation process in the Milky Way [54]. It is possible that the same interactions occur in the vicinities of GCR sources, particularly in the case that there are dense molecular clouds surrounding the sources. Such interactions were proposed to explain the positron excess [83–87], and the ultra-high-energy diffuse γ-ray emission measured by Tibet ASγ [88, 89]. To account for the positron excess, this new secondary component is required to be close to the Earth, and the time-dependent propagation is employed to suppress low-energy particles and to account for the measured high-energy excess of positrons. On the other hand, the general secondary interactions around sources can contribute to the high-energy positrons, but cannot fit the data nicely, and additional nearby source(s) (as also required by the primary GCR spectral features and anisotropies) is

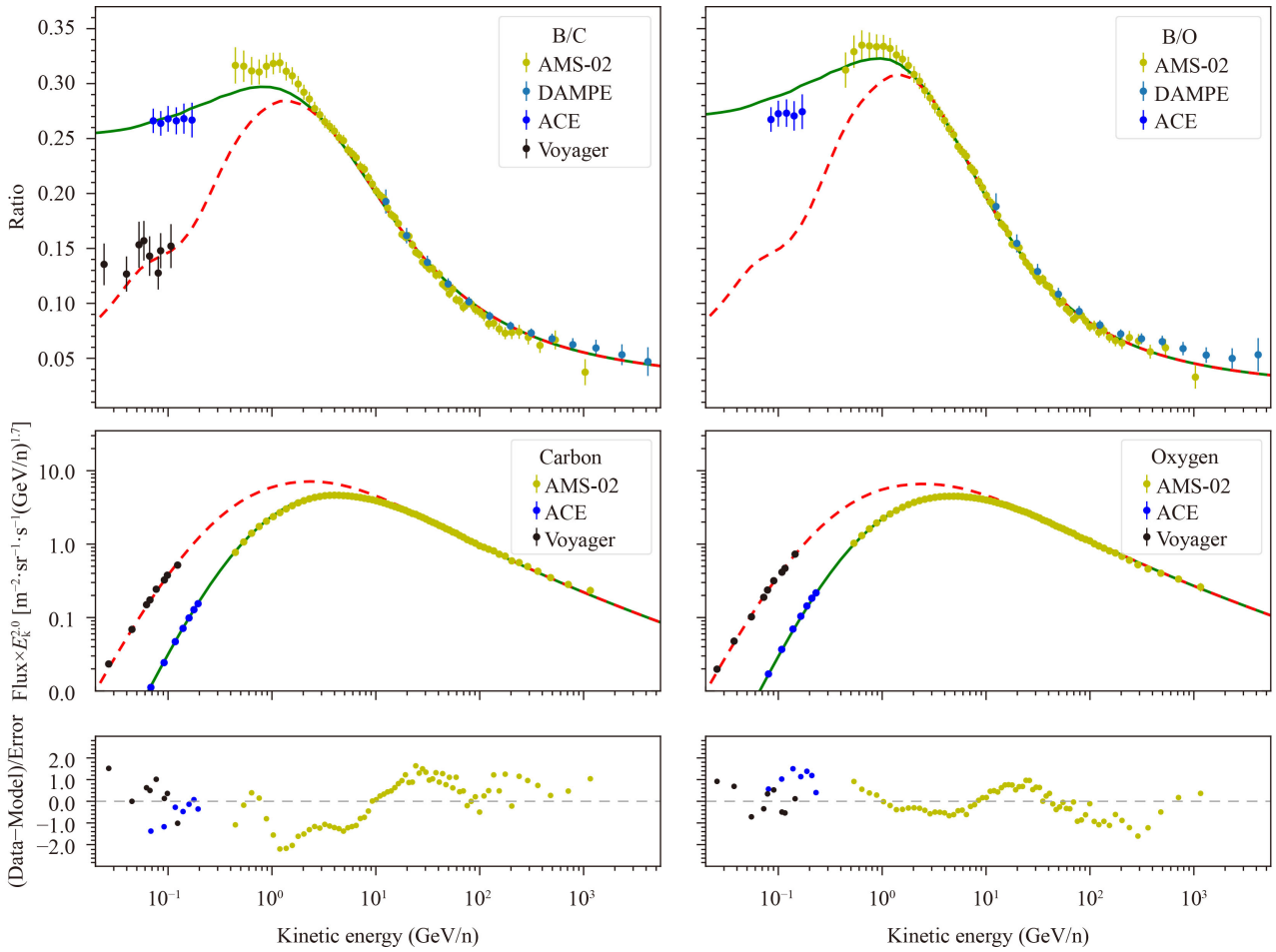

Fig. 4 B/C and B/O ratios (top panels), and C, O fluxes (bottom panels) for the spatially-dependent propagation model. Dashed lines are the spectra in the local ISM, and solid lines are modulated spectra near the Earth. Sub-panels of bottom ones show the residuals of the model fittings to the C and O spectra.

assumed [89].

Such interactions should imprint on the B/C and B/O ratios [89, 90]. Different from Refs. [89, 90], we investigate the effects from secondary interactions in both the ISM and the vicinities of the sources, without assuming the nearby source component. The hardenings of primary GCR spectra are assumed to be a source injection effect [44, 45]. The injection spectrum takes the form of Eq. (4), with $n = 2$. The secondary source function can be written as

$$q_{\mathrm{sec},j} = \sum_i (n_{\mathrm{H}}\sigma_{i+\mathrm{H}\to j} + n_{\mathrm{He}}\sigma_{i+\mathrm{He}\to j})v_i \times [\psi_i(\mathcal{R}) + q_i(\mathcal{R})\tau], \quad (9)$$

where i represents any species that can fragment into secondary particle j, and v_i is the velocity of the parent particle. The first term in the bracket represents the equilibrium density of parent GCRs after the propagation, while the second term is the contribution from secondary interactions around sources in which q_i is the injection source function, and τ is the interaction time scale.

We insert the $q_i(\mathcal{R})\tau$ term in the routine to calculate the secondary source function in GALPROP, and calculate its propagation simultaneously with the conventional secondary particles. The propagation and source parameters tuned to match the data are given in Table 2. The red thin lines in Fig. 6 show the results for the model predictions (labelled as model F), compared with the data. The $q_i(\mathcal{R})\tau$ term results in a flat secondary-to-primary ratio above a few GeV/n, while the ψ_i term gives a decreasing ratio. The sum of these two components naturally explains the hardenings of the B/C and B/O ratios. Note that the results of this scenario are similar with the NLB model, but with different physical meanings. In the NLB model, a rigidity-dependent escape is assumed in the vicinities of the sources, and a constant escape is assumed for the Milky Way propagation. Here, on the contrary, the Milky Way propagation is rigidity-dependent, and inside the source regions, confinements of both primary and secondary nuclei are assumed. The interaction time in this case is found to be 0.46 Myr.

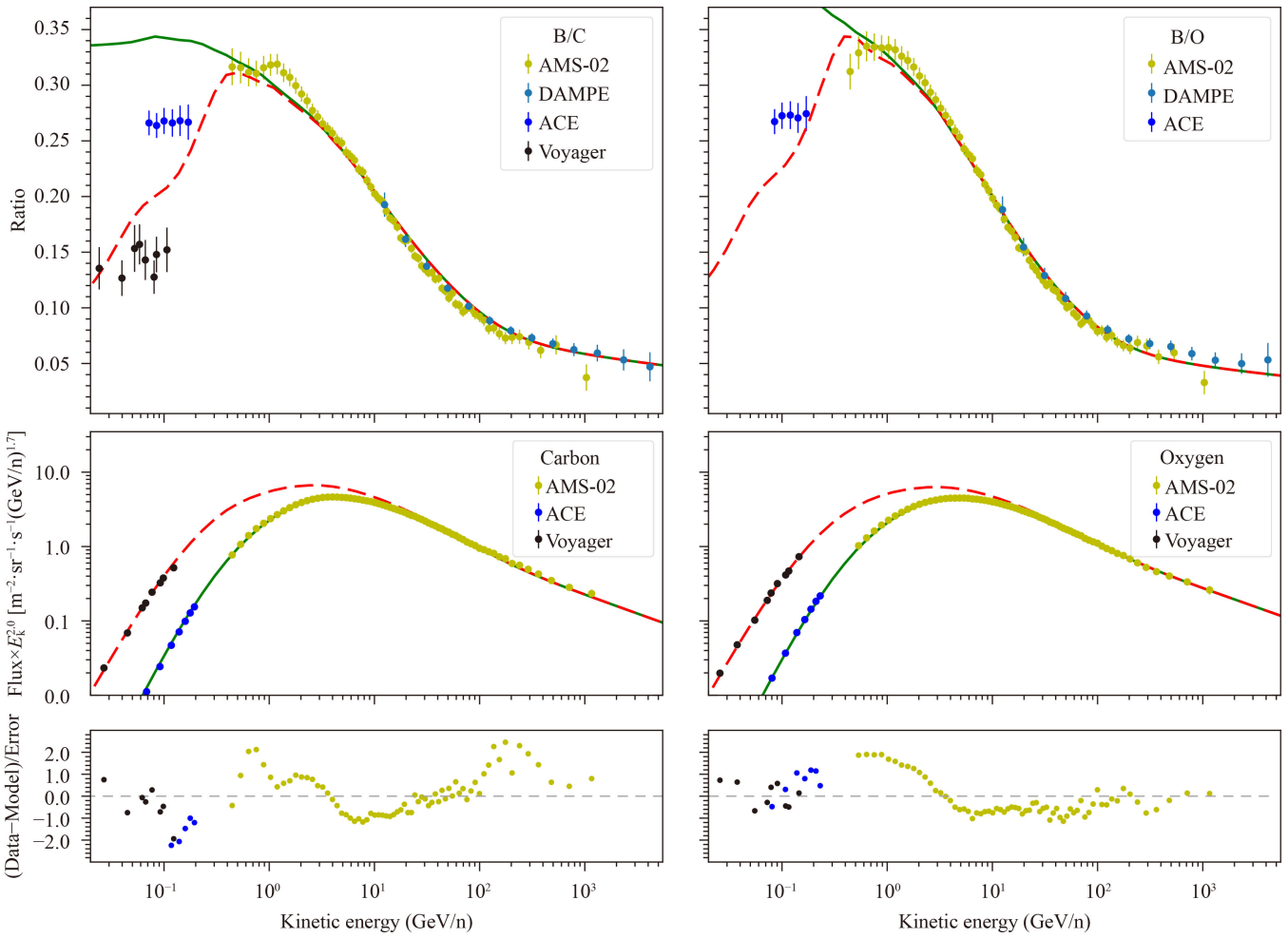

Fig. 5 B/C and B/O ratios (top panels), and C, O fluxes (bottom panels) for the Self-generated turbulence model. Dashed lines are the spectra in the local ISM, and solid lines are modulated spectra near the Earth. Sub-panels of bottom ones show the residuals of the model fittings to the C and O spectra.

This time scale is too long compared with the typical life time of supernova remnants ($< 10^5$ yr; [91]). If the sources are associated with molecular clouds in general, the required interaction time can be shorter.

3.7 Secondary production and acceleration at sources

Secondary particles generated close to the accelerating sources may have chance to be accelerated by the shocks of the sources, resulting in harder spectra of secondary particles than the primary particles, which can explain the positron excess [92–94]. The secondary-to-primary ratios of nuclei were shown to be sensitive probes of this model [51, 95, 96].

Assuming that the primary particles accelerated by the source have a power-law spectrum of $\mathcal{R}^{-\gamma}$, the spectrum of secondary particles can be expressed as the sum of two power-laws: one with approximate $\mathcal{R}^{-\gamma}$ spectrum describing the component advected away from the shock, and the other with approximate $\mathcal{R}^{-\gamma+\delta}$ is the component subject to additional acceleration by the shock [93, 97]. Here δ is the slope of the rigidity-dependence of the diffusion coefficient around the shock. For Bohm-like diffusion which corresponds to the regime that the mean free path of a particle is of the order of the gyroradius and is usually assumed for diffusive shock acceleration with a possible fudge factor (e.g., [92, 93]), $\delta = 1$. Therefore, we multiply a factor[6] $(1 + \mathcal{R}/\mathcal{R}_{\rm ac})$ to the propagated component of secondary particles produced at source. Here $\mathcal{R}_{\rm ac}$ is the characteristic rigidity that accelerated secondary particles become important. The parameter $\mathcal{R}_{\rm ac}$ depends on the diffusion coefficient and shock parameters, which can be derived via fitting to the B/C and B/O data.

The results for B/C, B/O, C and O fluxes for $\tau = 0.24$ Myr and $\mathcal{R}_{\rm ac} = 4$ TV are shown by green thick lines of

[6]The condition that the number of secondary particles being accelerated should not exceed the total number of secondaries limits the growth of the accelerated term. This affects the energy spectrum of secondary particles at a break rigidity above which the spectrum returns to $\mathcal{R}^{-\gamma}$ [93]. The break may occur at rigidities too high to be probed by the current data, and thus we do not consider it here.

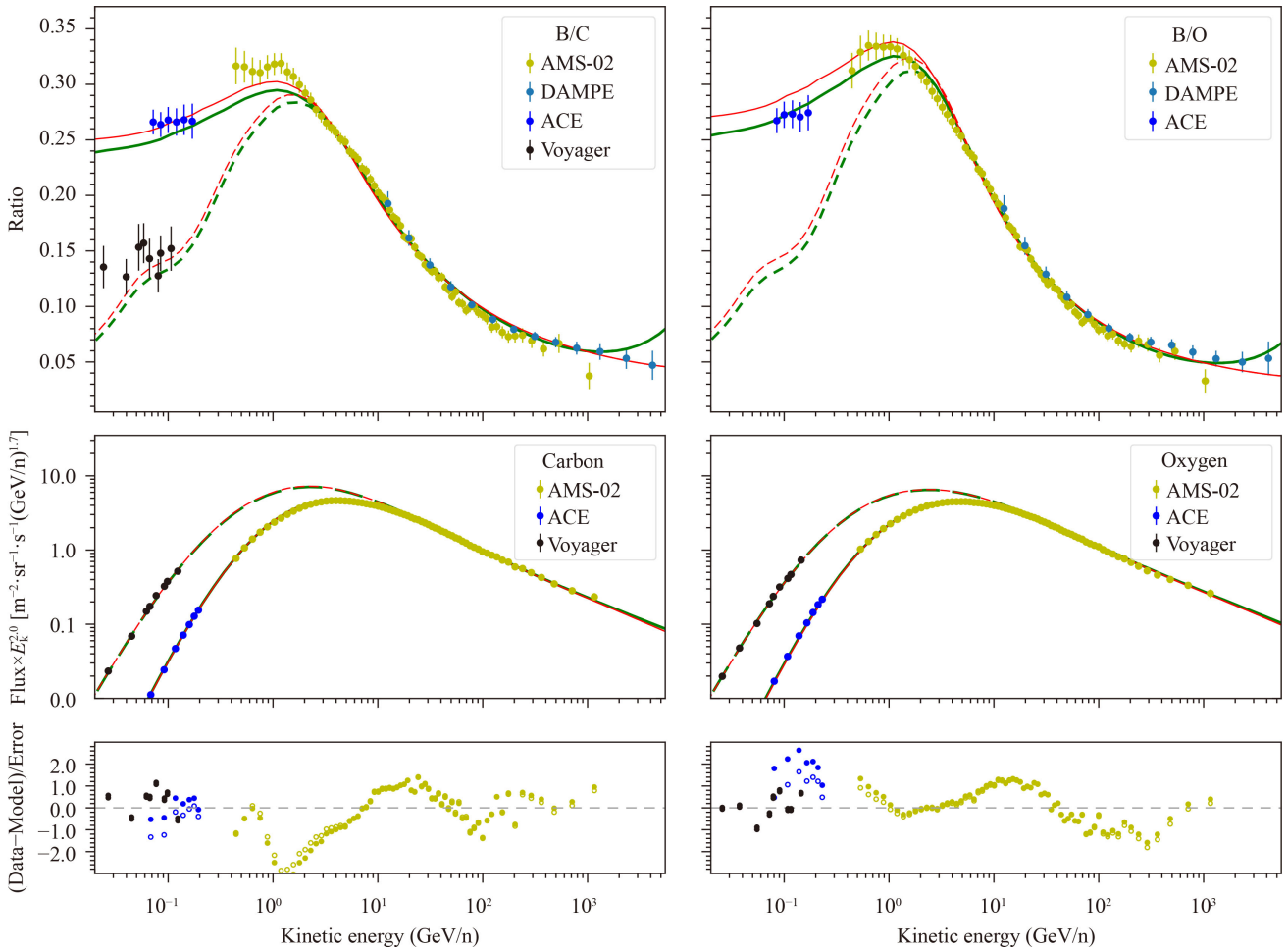

Fig. 6 B/C and B/O ratios (top panels), and C, O fluxes (bottom panels) for the models with secondary production (model F; red thin lines) and acceleration (model G; green thick lines) at source. Dashed lines are the spectra in the local ISM, and solid lines are modulated spectra near the Earth. Sub-panels of bottom ones show the residuals of the model fittings to the C and O spectra. The filled symbols are for model F and open symbols are for model G.

Fig. 6. Other parameters of this model (model G) are given in Table 2. Rising behaviors of the B/C and B/O ratios are predicted in this scenario. Since we do not observe such a rising in the DAMPE data, $\mathcal{R}_{ac}$ is constrained to be higher than previous works [51, 95, 96]. The parameter $\mathcal{R}_{ac}$ may be even higher if we require that there is no significant rising of the B/C ratio above 2 TeV/n. Then this model further degenerates with model F in the previous sub-section.

4 Implications on other secondary particles

The effects on the production of secondary boron nuclei are also expected to imprint on other secondary particles, such as antiprotons and positrons. Of particular interests is that antiprotons and positrons are widely employed to search for dark matter annihilation or decay. It is thus necessary to investigate how the change of the boron production or propagation affects the predictions of secondary antiprotons and positrons.

Using the propagation parameters given in Table 2, we adjust slightly the injection spectral parameters to match the wide-band measurements of protons and helium nuclei by Voyager, AMS-02, and DAMPE [14, 38, 41, 42, 99], and then calculate the spectra of antiprotons and positrons. The results are shown in Fig. 7. The left panels correspond to models B, B′, D, and E which represent the class driven by propagation effects, while the right panels correspond to models F and G which represent the class driven by source effects.

As can be seen from the plot, the propagation effect will in general result in a hardening of the antiproton spectrum above a few hundred GV rigidity, similar with the B/C and B/O ratios. The source effect is somehow different, due to different kinematics of the production of boron nuclei, antiprotons, and positrons. The inelasticity parameter, describing the fraction of energy of the parent particle carried away by the secondary particle, is about 1 for boron nuclei, 0.17 for antiprotons, and 0.05 for positrons. Therefore we see that the effect of

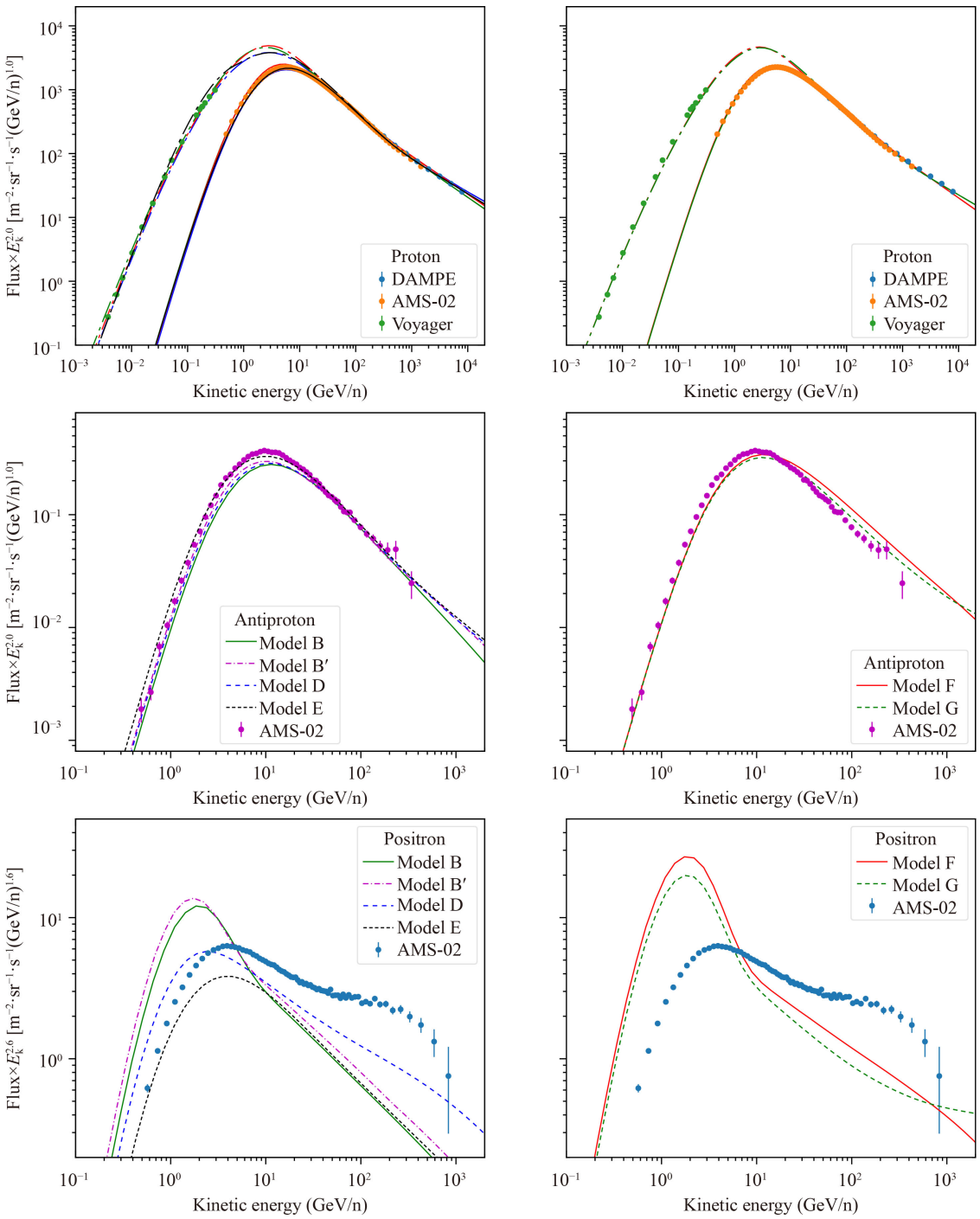

Fig. 7 Spectra of protons (top panels), antiprotons (middle panels), and positrons (bottom panels) for the model predictions, compared with the data [14, 41, 98–100]. The left panels show the predictions of models B, B′, D, E, and the right panels show the predictions of models F and G. The solar modulation potential is about 0.7 GV for all species.

secondary production at sources start to appear at lower energy for antiprotons than that for boron, which results in slight excess of antiprotons above 20 GeV. At low energies, we note that most of the model calculations are lower than measured antiproton fluxes[7]. This is consistent with previous studies that the model with significant re-acceleration would under-predict low-energy antiprotons [17, 103], likely due to a smaller δ value in such models. If the re-acceleration is weaker (model B′) or there is no re-acceleration (model E), the low-energy antiproton deficit is less significant. We should bear in mind that uncertainties of the inelastic hadronic interaction cross

[7]See for example, a dark matter annihilation explanation of this potential excess [101, 102].

section to produce antiprotons may need to be considered when quantitative comparisons are performed.

As for positrons, all the models predict lower positron fluxes than the AMS-02 measurements [100] above ~ 10 GeV, indicating that additional positron sources are required. For $E \lesssim 10$ GeV, the re-acceleration models typically over-predict positrons, consistent with previous studies [17, 64]. For models D and E, less prominent bumps are given due to a smaller re-acceleration term. We note that the spatially-dependent propagation model (model D) predicts harder positron spectrum than other models. This is mainly because the competition between diffusion and cooling is different for the disk and halo regions in this model. In the disk the diffusion coefficient is very small, and the cooling effect dominates the propagation, which results in a soft positron spectrum. On the other hand, the diffusion becomes much more important in the halo, which results in a harder spectrum. The hard spectrum thus reflects the fast diffusion in the Galactic halo.

5 Conclusion

In this work we study a series of revised models of the standard GCR propagation in light of new measurements of B/C and B/O ratios by DAMPE which firmly established hardenings of both ratios around 100 GeV/n [35]. These models, as detailed in Section 3, rely on different physical assumptions and turn out to modify the propagation process (models A, B, B′, C, D, E) or production of secondary particles (models F, G) based on the conventional paradigm. Our conclusion can be summarized as follows.

- About half of the models (B′, D, F, and G) can properly reproduce the B/C and B/O ratios as well as C, O fluxes in a wide energy range from 0.01 GeV/n to 5 TeV/n. For the NLB model (A) and re-acceleration by a local shock model (C) we only compare them with the data above 25 GeV/n, and for the self-generated turbulence model (E) we do not tune the results below ~ 3 GeV/n. The re-acceleration model (B) is not enough to give the prominent hardenings of the B/C and B/O ratios revealed by DAMPE. The model of production and acceleration of secondary particles at source (G) predicts rising behavior of the ratios at high energies, which is not shown by the current data.
- The models with significant re-acceleration (a large v_A; B, B′, F, G) under-predict low energy antiprotons, but over-predict low-energy positrons.
- The models with secondary production at sources (without and with acceleration) over-predict high-energy antiprotons.
- For all the models discussed in this work, high-energy positron excess still exists, which requires additional sources of positrons.

It is shown that the new measurements of GCR spectra and ratios in recent years can indeed provide important constraints on the propagation and interaction of GCRs in the Milky Way. Additional tests of these models may include the anisotropies of GCRs and wide-band diffuse γ-rays. In addition, the uncertainties from nuclear and particle physics become more and more prominent when making precise comparisons between model predictions and the astroparticle data, particularly for the search for dark matter.

Acknowledgements This work was supported by the National Key Research and Development Program of China (No. 2021YFA0718404), the National Natural Science Foundation of China (Nos. 12220101003 and 12103094), and the Project for Young Scientists in Basic Research of Chinese Academy of Sciences (No. YSBR-061). The calculation was partially done on the Cosmology Simulation Database (CSD) of the National Basic Science Data Center (NBSDC-DB-10).

References

1. T. K. Gaisser, Cosmic Rays and Particle Physics, Cambridge and New York: Cambridge University Press, 1990
2. V. S. Berezinskii, S. V. Bulanov, V. A. Dogiel, and V. S. Ptuskin, Astrophysics of Cosmic Rays, Amsterdam: North Holland, 1990, edited by V. L. Ginzburg, 1990
3. V. L. Ginzburg and S. I. Syrovatskii, The Origin of Cosmic Rays, New York: Macmillan, 1964
4. M. Aguilar, L. Ali Cavasonza, G. Ambrosi, L. Arruda, N. Attig, et al., Observation of new properties of secondary cosmic rays lithium, beryllium, and boron by the alpha magnetic spectrometer on the International Space Station, *Phys. Rev. Lett.* 120(2), 021101 (2018)
5. J. J. Engelmann, P. Ferrando, A. Soutoul, P. Goret, and E. Juliusson, Charge composition and energy spectra of cosmic-ray nuclei for elements from Be to NI - Results from HEAO-3-C2, *Astron. Astrophys.* 233, 96 (1990)
6. S. P. Swordy, D. Mueller, P. Meyer, J. L'Heureux, and J. M. Grunsfeld, Relative abundances of secondary and primary cosmic rays at high energies, *Astrophys. J.* 349, 625 (1990)
7. M. Aguilar, J. Alcaraz, J. Allaby, B. Alpat, G. Ambrosi, et al., Relative composition and energy spectra of light nuclei in cosmic rays: Results from AMS-01, *Astrophys. J.* 724(1), 329 (2010)
8. A. D. Panov, et al., Relative abundances of cosmic ray nuclei B-C-N-O in the energy region from 10 GeV/n to 300 GeV/n, Results from ATIC-2 (the science flight of ATIC), in: *International Cosmic Ray Conference*, International Cosmic Ray Conference, Vol. 2 (2008), pp 3–6, arXiv: 0707.4415
9. H. S. Ahn, P. S. Allison, M. G. Bagliesi, J. J. Beatty, G. Bigongiari, et al., Measurements of cosmic-ray secondary nuclei at high energies with the first flight of the CREAM balloon-borne experiment, *Astropart.*

Phys. 30(3), 133 (2008)
10. A. Obermeier, M. Ave, P. Boyle, C. Höppner, J. Hörandel, and D. Müller, Energy spectra of primary and secondary cosmic-ray nuclei measured with TRACER, *Astrophys. J.* 742(1), 14 (2011)
11. O. Adriani, G. C. Barbarino, G. A. Bazilevskaya, R. Bellotti, M. Boezio, et al., Measurement of boron and carbon fluxes in cosmic rays with the PAMELA experiment, *Astrophys. J.* 791(2), 93 (2014)
12. M. Aguilar, L. Ali Cavasonza, G. Ambrosi, L. Arruda, N. Attig, et al., Precise measurement of the boron to carbon flux ratio in cosmic rays from 1.9 GV to 2.6 TV with the alpha magnetic spectrometer on the International Space Station, *Phys. Rev. Lett.* 117(23), 231102 (2016)
13. V. Grebenyuk, D. Karmanov, I. Kovalev, I. Kudryashov, A. Kurganov, A. Panov, D. Podorozhny, A. Tkachenko, L. Tkachev, A. Turundaevskiy, O. Vasiliev, and A. Voronin, Secondary cosmic rays in the NUCLEON space experiment, *Adv. Space Res.* 64(12), 2559 (2019)
14. A. C. Cummings, E. C. Stone, B. C. Heikkila, N. Lal, W. R. Webber, G. Johannesson, I. V. Moskalenko, E. Orlando, and T. A. Porter, Galactic cosmic rays in the local interstellar medium: Voyager 1 observations and model results, *Astrophys. J.* 831(1), 18 (2016)
15. P. Ferrando, N. Lal, F. B. McDonald, and W. R. Webber, Studies of low-energy Galactic cosmic-ray composition at 22 AU. I — Secondary/primary ratios, *Astron. Astrophys.* 247(1), 163 (1991)
16. J. S. George, K. A. Lave, M. E. Wiedenbeck, W. R. Binns, A. C. Cummings, A. J. Davis, G. A. de Nolfo, P. L. Hink, M. H. Israel, R. A. Leske, R. A. Mewaldt, L. M. Scott, E. C. Stone, T. T. von Rosenvinge, and N. E. Yanasak, Elemental composition and energy spectra of Galactic cosmic rays during solar cycle 23, *Astrophys. J.* 698(2), 1666 (2009)
17. Q. Yuan, S. J. Lin, K. Fang, and X. J. Bi, Propagation of cosmic rays in the AMS-02 era, *Phys. Rev. D* 95(8), 083007 (2017)
18. A. W. Strong and I. V. Moskalenko, Propagation of cosmic-ray nucleons in the Galaxy, *Astrophys. J.* 509(1), 212 (1998)
19. J. Feng, N. Tomassetti, and A. Oliva, Bayesian analysis of spatial-dependent cosmic-ray propagation: Astrophysical background of antiprotons and positrons, *Phys. Rev. D* 94(12), 123007 (2016)
20. D. Mueller, S. P. Swordy, P. Meyer, J. L'Heureux, and J. M. Grunsfeld, Energy spectra and composition of primary cosmic rays, *Astrophys. J.* 374, 356 (1991)
21. D. Maurin, F. Donato, R. Taillet, and P. Salati, Cosmic rays below $Z = 30$ in a diffusion model: New constraints on propagation parameters, *Astrophys. J.* 555(2), 585 (2001)
22. M. Ave, P. J. Boyle, C. Hoppner, J. Marshall, and D. Müller, Propagation and source energy spectra of cosmic ray nuclei at high energies, *Astrophys. J.* 697(1), 106 (2009)
23. A. Putze, L. Derome, and D. Maurin, A Markov chain Monte Carlo technique to sample transport and source parameters of Galactic cosmic rays (II): Results for the diffusion model combining B/C and radioactive nuclei, *Astron. Astrophys.* 516, A66 (2010)
24. R. Trotta, G. Johannesson, I. V. Moskalenko, T. A. Porter, R. Ruiz de Austri, and A. W. Strong, Constraints on cosmic ray propagation models from a global Bayesian analysis, *Astrophys. J.* 729(2), 106 (2011)
25. A. Obermeier, P. Boyle, J. Horandel, and D. Müller, The boron-to-carbon abundance ratio and Galactic propagation of cosmic radiation, *Astrophys. J.* 752(1), 69 (2012)
26. H. B. Jin, Y. L. Wu, and Y. F. Zhou, Cosmic ray propagation and dark matter in light of the latest AMS-02 data, *J. Cosmol. Astropart. Phys.* 9, 049 (2015)
27. G. Jóhannesson, R. R. Austri, A. C. Vincent, I. V. Moskalenko, E. Orlando, T. A. Porter, A. W. Strong, R. Trotta, F. Feroz, P. Graff, and M. P. Hobson, Bayesian analysis of cosmic ray propagation: Evidence against homogeneous diffusion, *Astrophys. J.* 824(1), 16 (2016)
28. M. Korsmeier and A. Cuoco, Galactic cosmic-ray propagation in the light of AMS-02: Analysis of protons, helium, and antiprotons, *Phys. Rev. D* 94(12), 123019 (2016)
29. J. S. Niu and T. Li, Galactic cosmic-ray model in the light of AMS-02 nuclei data, *Phys. Rev. D* 97(2), 023015 (2018)
30. J. Wu and H. Chen, Revisit cosmic ray propagation by using ^{1}H, ^{2}H, ^{3}He and ^{4}He, *Phys. Lett. B* 789, 292 (2019)
31. A. Kolmogorov, The local structure of turbulence in incompressible viscous fluid for very large Reynolds' numbers, *Akademiia Nauk SSSR Doklady* 30, 301 (1941)
32. M. Aguilar, L. Ali Cavasonza, G. Ambrosi, L. Arruda, N. Attig, et al., The Alpha Magnetic Spectrometer (AMS) on the international space station (Part II): Results from the first seven years, *Phys. Rep.* 894, 1 (2021)
33. J. Chang, Dark matter particle explorer: The first Chinese cosmic ray and hard gamma-ray detector in space, *Chin. J. Space Sci.* 34, 550 (2014)
34. J. Chang, G. Ambrosi, Q. An, R. Asfandiyarov, P. Azzarello, et al., The DArk matter particle explorer mission, *Astropart. Phys.* 95, 6 (2017)
35. F. Alemanno, et al., Detection of spectral hardenings in cosmic-ray boron-to-carbon and boron-to-oxygen flux ratios with DAMPE, *Sci. Bull. (Beijing)* 67(21), 2162 (2022)
36. A. D. Panov, J. H. Jr Adams, H. S. Ahn, G. L. Bashinzhagyan, J. W. Watts, J. P. Wefel, J. Wu, O. Ganel, T. G. Guzik, V. I. Zatsepin, I. Isbert, K. C. Kim, M. Christl, E. N. Kouznetsov, M. I. Panasyuk, E. S. Seo, N. V. Sokolskaya, J. Chang, W. K. H. Schmidt, and A. R. Fazely, Energy spectra of abundant nuclei of primary cosmic rays from the data of ATIC-2 experiment: Final results, *Bull. Russ. Acad. Sci. Physics* 73(5), 564 (2009)
37. H. S. Ahn, P. Allison, M. G. Bagliesi, J. J. Beatty, G. Bigongiari, et al, Discrepant hardening observed in

cosmic ray elemental spectra, *Astrophys. J. Lett.* 714(1), L89 (2010)
38. M. Aguilar, L. Ali Cavasonza, B. Alpat, G. Ambrosi, L. Arruda, et al., Observation of the identical rigidity dependence of He, C, and O cosmic rays at high rigidities by the alpha magnetic spectrometer on the International Space Station, *Phys. Rev. Lett.* 119(25), 251101 (2017)
39. O. Adriani, Y. Akaike, K. Asano, Y. Asaoka, M. G. Bagliesi, et al., Direct measurement of the cosmic-ray carbon and oxygen spectra from 10 GeV/n to 2.2 TeV/n with the calorimetric electron telescope on the International Space Station, *Phys. Rev. Lett.* 125(25), 251102 (2020)
40. O. Adriani, G. C. Barbarino, G. A. Bazilevskaya, R. Bellotti, M. Boezio, et al., PAMELA measurements of cosmic-ray proton and helium spectra, *Science* 332(6025), 69 (2011)
41. Q. An, R. Asfandiyarov, P. Azzarello, P. Bernardini, X. J. Bi, et al., Measurement of the cosmic ray proton spectrum from 40 GeV to 100 TeV with the DAMPE satellite, *Sci. Adv.* 5(9), eaax3793 (2019)
42. F. Alemanno, Q. An, P. Azzarello, F. C. T. Barbato, P. Bernardini, et al., Measurement of the cosmic ray helium energy spectrum from 70 GeV to 80 TeV with the DAMPE space mission, *Phys. Rev. Lett.* 126(20), 201102 (2021)
43. Y. Génolini, P. D. Serpico, M. Boudaud, S. Caroff, V. Poulin, L. Derome, J. Lavalle, D. Maurin, V. Poireau, S. Rosier, P. Salati, and M. Vecchi, Indications for a high-rigidity break in the cosmic-ray diffusion coefficient, *Phys. Rev. Lett.* 119(24), 241101 (2017)
44. A. E. Vladimirov, G. Johannesson, I. V. Moskalenko, and T. A. Porter, Testing the origin of high-energy cosmic rays, *Astrophys. J.* 752(1), 68 (2012)
45. M. J. Boschini, S. D. Torre, M. Gervasi, D. Grandi, G. Jóhannesson, G. L. Vacca, N. Masi, I. V. Moskalenko, S. Pensotti, T. A. Porter, L. Quadrani, P. G. Rancoita, D. Rozza, and M. Tacconi, Inference of the local interstellar spectra of cosmic-ray nuclei $Z \leq 28$ with the GALPROPHELMOD framework, *Astrophys. J. Suppl. Ser.* 250(2 Suppl.), 27 (2020)
46. P. Blasi, E. Amato, and P. D. Serpico, Spectral breaks as a signature of cosmic ray induced turbulence in the Galaxy, *Phys. Rev. Lett.* 109(6), 061101 (2012)
47. R. Cowsik and T. Madziwa-Nussinov, Spectral intensities of antiprotons and the nested leaky-box model for cosmic rays in the Galaxy, *Astrophys. J.* 827(2), 119 (2016)
48. Q. Yuan, C.-R. Zhu, X.-J. Bi, and D.-M. Wei, Secondary cosmic-ray nucleus spectra disfavor particle transport in the Galaxy without reacceleration, *J. Cosmol. Astropart. Phys.* 2020, 027 (2020)
49. M. A. Malkov and I. V. Moskalenko, On the origin of observed cosmic-ray spectrum below 100 TV, *Astrophys. J.* 933(1), 78 (2022)
50. Y. Q. Guo and Q. Yuan, Understanding the spectral hardenings and radial distribution of Galactic cosmic rays and Fermi diffuse γ rays with spatially-dependent propagation, *Phys. Rev. D* 97(6), 063008 (2018)
51. P. Mertsch, A. Vittino, and S. Sarkar, Explaining cosmic ray antimatter with secondaries from old supernova remnants, *Phys. Rev. D* 104(10), 103029 (2021)
52. V. Bresci, E. Amato, P. Blasi, and G. Morlino, Effects of reacceleration and source grammage on secondary cosmic rays spectra, *Mon. Not. R. Astron. Soc.* 488(2), 2068 (2019)
53. N. Kawanaka and S. H. Lee, Origin of spectral hardening of secondary cosmic-ray nuclei, *Astrophys. J.* 917(2), 61 (2021)
54. A. W. Strong, I. V. Moskalenko, and V. S. Ptuskin, Cosmic-ray propagation and interactions in the Galaxy, *Annu. Rev. Nucl. Part. Sci.* 57(1), 285 (2007)
55. Q. Yuan, Implications on cosmic ray injection and propagation parameters from Voyager/ACE/AMS-02 nucleus data, *Sci. China Phys. Mech. Astron.* 62(4), 49511 (2019)
56. E. S. Seo and V. S. Ptuskin, Stochastic reacceleration of cosmic rays in the interstellar medium, *Astrophys. J.* 431, 705 (1994)
57. T. A. Porter, G. Johannesson, and I. V. Moskalenko, The GALPROP cosmic-ray propagation and nonthermal emissions framework: Release v57, *Astrophys. J. Suppl. Ser.* 262(1 Suppl.), 30 (2022)
58. L. J. Gleeson and W. I. Axford, Solar Modulation of Galactic Cosmic Rays, *Astrophys. J.* 154, 1011 (1968)
59. M. J. Boschini, S. Della Torre, M. Gervasi, G. La Vacca, and P. G. Rancoita, The transport of Galactic cosmic rays in heliosphere: The HELMOD model compared with other commonly employed solar modulation models, *Adv. Space Res.* 70(9), 2636 (2022)
60. R. Cowsik and L. W. Wilson, Is the residence time of cosmic rays in the Galaxy energy-dependent? in: *International Cosmic Ray Conference*, International Cosmic Ray Conference, Vol. 1 (1973), p. 500
61. R. Cowsik and B. Burch, Positron fraction in cosmic rays and models of cosmic-ray propagation, *Phys. Rev. D* 82(2), 023009 (2010)
62. Y. Génolini, D. Maurin, I. V. Moskalenko, and M. Unger, Current status and desired precision of the isotopic production cross sections relevant to astrophysics of cosmic rays: Li, Be, B, C, and N, *Phys. Rev. C* 98(3), 034611 (2018)
63. I. V. Moskalenko, A. E. Vladimirov, T. A. Porter, and A. W. Strong, Isotopic Production Cross Sections for CR Applications (ISOPROCS Project), in: *International Cosmic Ray Conference*, International Cosmic Ray Conference, Vol. 33 (2013), p. 803
64. I. V. Moskalenko, A. W. Strong, J. F. Ormes, and M. S. Potgieter, Secondary antiprotons and propagation of cosmic rays in the Galaxy and heliosphere, *Astrophys. J.* 565(1), 280 (2002)
65. A. Lukasiak, Voyager measurements of the charge and isotopic composition of cosmic ray Li, Be and B nuclei and implications for their production in the Galaxy, in: *International Cosmic Ray Conference*, Vol. 3 (1999), p. 41
66. N. E. Yanasak, M. E. Wiedenbeck, R. A. Mewaldt, A. J. Davis, A. C. Cummings, J. S. George, R. A. Leske, E. C. Stone, E. R. Christian, T. T. von Rosenvinge, W. R. Binns, P. L. Hink, and M. H. Israel, Measurement of the secondary radionuclides ^{10}Be, ^{26}Al, ^{36}Cl, ^{54}Mn, and ^{14}C and implications for the Galactic cosmic-ray

age, *Astrophys. J.* 563(2), 768 (2001)
67. J. A. Simpson and M. Garcia-Munoz, Cosmic-ray lifetime in the Galaxy — Experimental results and models, *Space Sci. Rev.* 46(3–4), 205 (1988)
68. J. J. Connell, Galactic cosmic-ray confinement time: ULYSSES high energy telescope measurements of the secondary radionuclide ^{10}Be, *Astrophys. J.* 501(1), L59 (1998)
69. T. Hams, L. M. Barbier, M. Bremerich, E. R. Christian, G. A. de Nolfo, S. Geier, H. Gobel, S. K. Gupta, M. Hof, W. Menn, R. A. Mewaldt, J. W. Mitchell, S. M. Schindler, M. Simon, and R. E. Streitmatter, Measurement of the abundance of radioactive ^{10}Be and other light isotopes in cosmic radiation up to 2 GeV nucleon-1 with the balloon-borne instrument ISOMAX, *Astrophys. J.* 611(2), 892 (2004)
70. D. Foreman-Mackey, D. W. Hogg, D. Lang, and J. Goodman, emcee: The MCMC hammer, *Publ. Astron. Soc. Pac.* 125(925), 306 (2013), doi: 10.1086/670067
71. M. A. Malkov and I. V. Moskalenko, The TeV cosmic-ray bump: A message from the Epsilon Indi or Epsilon Eridani star, *Astrophys. J.* 911(2), 151 (2021)
72. M. Ackermann, M. Ajello, W. B. Atwood, L. Baldini, J. Ballet, et al., Fermi-LAT observations of the diffuse γ-ray emission: Implications for cosmic rays and the interstellar medium, *Astrophys. J.* 750(1), 3 (2012)
73. A. U. Abeysekara, A. Albert, R. Alfaro, C. Alvarez, J. D. Álvarez, et al., Extended gamma-ray sources around pulsars constrain the origin of the positron flux at Earth, *Science* 358(6365), 911 (2017)
74. F. Aharonian, Q. An, Axikegu, L. X. Bai, Y. X. Bai, et al., Extended very-high-energy gamma-ray emission surrounding PSR J 0622 +3749 observed by LHAASO-KM2A, *Phys. Rev. Lett.* 126(24), 241103 (2021)
75. D. Hooper, I. Cholis, T. Linden, and K. Fang, HAWC observations strongly favor pulsar interpretations of the cosmic-ray positron excess, *Phys. Rev. D* 96(10), 103013 (2017)
76. K. Fang, X. J. Bi, P. F. Yin, and Q. Yuan, Two-zone diffusion of electrons and positrons from Geminga explains the positron anomaly, *Astrophys. J.* 863(1), 30 (2018)
77. N. Tomassetti, Origin of the cosmic-ray spectral hardening, *Astrophys. J. Lett.* 752(1), L13 (2012)
78. B. Q. Qiao, W. Liu, M. J. Zhao, X. J. Bi, and Y. Q. Guo, Galactic cosmic ray propagation: sub-PeV diffuse gammaray and neutrino emission, *Front. Phys.* 17(4), 44501 (2022)
79. M. J. Zhao, K. Fang, and X. J. Bi, Constraints on the spatially dependent cosmic-ray propagation model from Bayesian analysis, *Phys. Rev. D* 104(12), 123001 (2021)
80. Y. Q. Guo, Z. Tian, and C. Jin, Spatial-dependent propagation of cosmic rays results in the spectrum of proton, ratios of P/P, and B/C, and anisotropy of nuclei, *Astrophys. J.* 819(1), 54 (2016)
81. J. Skilling, Cosmic rays in the Galaxy: Convection or diffusion, *Astrophys. J.* 170, 265 (1971)
82. S. Recchia, P. Blasi, and G. Morlino, On the radial distribution of Galactic cosmic rays, *Mon. Not. R. Astron. Soc.* 462(1), L88 (2016)
83. Y. Fujita, K. Kohri, R. Yamazaki, and K. Ioka, Is the PAMELA anomaly caused by supernova explosions near the Earth, *Phys. Rev. D* 80(6), 063003 (2009)
84. W. Liu, X. J. Bi, S. J. Lin, B. B. Wang, and P. F. Yin, Excesses of cosmic ray spectra from a single nearby source, *Phys. Rev. D* 96(2), 023006 (2017)
85. R. Yang and F. Aharonian, Interpretation of the excess of antiparticles within a modified paradigm of Galactic cosmic rays, *Phys. Rev. D* 100(6), 063020 (2019)
86. M. A. Malkov, P. H. Diamond, and R. Z. Sagdeev, Positive charge prevalence in cosmic rays: Room for dark matter in the positron spectrum, *Phys. Rev. D* 94(6), 063006 (2016)
87. K. Kohri, K. Ioka, Y. Fujita, and R. Yamazaki, Can we explain AMS-02 antiproton and positron excesses simultaneously by nearby supernovae without pulsars or dark matter, *Prog. Theor. Exper. Phys.* 2016, 021E01 (2016)
88. M. Amenomori, Y. W. Bao, X. J. Bi, D. Chen, T. L. Chen, et al., First detection of sub-PeV diffuse gamma rays from the Galactic disk: Evidence for ubiquitous Galactic cosmic rays beyond PeV energies, *Phys. Rev. Lett.* 126(14), 141101 (2021)
89. P. P. Zhang, B. Q. Qiao, Q. Yuan, S. W. Cui, and Y. Q. Guo, Ultrahigh-energy diffuse gamma-ray emission from cosmic-ray interactions with the medium surrounding acceleration sources, *Phys. Rev. D* 105(2), 023002 (2022)
90. P. P. Zhang, X. Y. He, W. Liu, and Y. Q. Guo, Evidence of fresh cosmic ray in Galactic plane based on DAMPE measurement of B/C and B/O ratios, *J. Cosmol. Astropart. Phys.* 02, 007 (2023)
91. H. Zeng, Y. Xin, and S. Liu, Evolution of high-energy particle distribution in supernova remnants, *Astrophys. J.* 874(1), 50 (2019)
92. P. Blasi, Origin of the positron excess in cosmic rays, *Phys. Rev. Lett.* 103(5), 051104 (2009)
93. M. Ahlers, P. Mertsch, and S. Sarkar, Cosmic ray acceleration in supernova remnants and the FERMI/PAMELA data, *Phys. Rev. D* 80(12), 123017 (2009)
94. E. G. Berezhko, L. T. Ksenofontov, V. S. Ptuskin, V. N. Zirakashvili, and H. J. Volk, Cosmic ray production in super-nova remnants including reacceleration: The secondary to primary ratio, *Astron. Astrophys.* 410(1), 189 (2003)
95. P. Mertsch and S. Sarkar, Testing astrophysical models for the PAMELA positron excess with cosmic ray nuclei, *Phys. Rev. Lett.* 103(8), 081104 (2009)
96. I. Cholis and D. Hooper, Constraining the origin of the rising cosmic ray positron fraction with the boron-to-carbon ratio, *Phys. Rev. D* 89(4), 043013 (2014)
97. P. Blasi and P. D. Serpico, High-energy antiprotons from old supernova remnants, *Phys. Rev. Lett.* 103(8), 081103 (2009)
98. M. Aguilar, L. Ali Cavasonza, B. Alpat, G. Ambrosi, L. Arruda, et al., Antiproton flux, antiproton-to-proton flux ratio, and properties of elementary particle fluxes in primary cosmic rays measured with the alpha magnetic spectrometer on the International Space Station, *Phys. Rev. Lett.* 117(9), 091103 (2016)

99. M. Aguilar, D. Aisa, B. Alpat, A. Alvino, G. Ambrosi, et al., Precision measurement of the proton flux in primary cosmic rays from rigidity 1 GV to 1.8 TV with the alpha magnetic spectrometer on the International Space Station, *Phys. Rev. Lett.* 114(17), 171103 (2015)
100. M. Aguilar, L. Ali Cavasonza, G. Ambrosi, L. Arruda, N. Attig, et al., Towards understanding the origin of cosmic-ray positrons, *Phys. Rev. Lett.* 122(4), 041102 (2019)
101. M. Y. Cui, Q. Yuan, Y. L. Sming Tsai, and Y. Z. Fan, A possible dark matter annihilation signal in the AMS-02 antiproton data, *Phys. Rev. Lett.* 118(19), 191101 (2017)
102. Y. Z. Fan, T. P. Tang, Y. L. S. Tsai, and L. Wu, Inert Higgs dark matter for CDF II W — Boson mass and detection prospects, *Phys. Rev. Lett.* 129(9), 091802 (2022)
103. I. V. Moskalenko, A. W. Strong, S. G. Mashnik, and J. F. Ormes, Challenging cosmic-ray propagation with antiprotons: Evidence for a "fresh" nuclei component, *Astrophys. J.* 586(2), 1050 (2003)